J Mater Sci (2010) 45:3635–3651
DOI 10.1007/s10853-010-4409-4

Shock deformation of coarse grain alumina above Hugoniot elastic limit

Anoop K. Mukhopadhyay · Keshaw D. Joshi · Arjun Dey · Riya Chakraborty · Amit Rav · Sampad K. Biswas · Satish C. Gupta

Received: 30 November 2009 / Accepted: 11 March 2010 / Published online: 24 March 2010

Abstract Symmetric shock experiments were conducted on a 10 μm grain size coarse alumina ceramic with a gas gun to identify its Hugoniot elastic limit (HEL). To understand the damage initiation and their subsequent growth mechanisms in coarse grain alumina subjected to shock impact at levels much above the HEL, additional asymmetric shock recovery experiments with the same gas gun were then deliberately conducted on the same alumina at shock pressure levels more than three times as high as the HEL and the fragments collected by a dedicated catcher system. Detailed characterization of the shock recovered alumina fragments by X-ray diffraction, nanoindentation, scanning electron microscopy, field emission scanning electron microscopy and transmission electron microscopy were utilized to understand the nature and process of failure initiation, incubational growth, coalescence and propagation leading to fragmentation. Based on these data a new qualitative damage model was developed to explain the deformation mechanism.

A. K. Mukhopadhyay (✉) · A. Dey · R. Chakraborty
Mechanical Property Evaluation Section, Central Glass and Ceramic Research Institute, Council of Scientific and Industrial Research, 196, Raja S.C. Mullick Road, Kolkata 700032, India
e-mail: anoopmukherjee@cgcri.res.in

S. K. Biswas
Non-Oxide Ceramic and Composite Division, Central Glass and Ceramic Research Institute, Council of Scientific and Industrial Research, Kolkata 700032, USA

K. D. Joshi · A. Rav · S. C. Gupta
Applied Physics Division, Bhabha Atomic Research Centre, Mumbai 400085, India

Introduction

Over the past about four decades or so, the dynamic response of brittle, strong ceramics, e.g. alumina to shock wave loading has been addressed by many researchers [1–21]. In spite of the wealth of literature, however, a fully physically based model is yet to emerge [1]. Thus the situation demands development of deeper understanding of the operative physical mechanisms as well as application of appropriate experimental method, e.g. soft recovery techniques [2, 20] to get further insight into the details of damage evolution and accumulation processes during shock wave propagation in ceramics. However, the lion's share of Hugoniot elastic limit (HEL) data is available only for fine grain sizes [1, 2] and data on coarse grain size are really rare [3]. Other researchers found that HEL ($\sim$2–10 GPa) was sensitive to relative density [4], grain size and porosity [6] of alumina but the presence of precursor decay in shock experiments could not be unequivocally established [3, 5–9, 21]. Fragmentation behaviour of alumina of 92–98.5% relative density correlated well with the toughness values [10]. Compressive failure of high purity, fine grain alumina was linked to development of basal twins [2], tensile stress field creating microcracks due to dislocation pile-ups [11, 12], time-dependent fracture and rate-dependent plasticity [13] and grain boundary microcracking [14]. Planar impact experiments with and without lateral confinement showed that brittle to ductile response can occur in alumina at HEL [15, 21]. Modified split Hopkinson pressure bar (SHPB) experiments used to load high purity, fine grain alumina by two consecutive shock pressure pulses showed that the compressive strengths of damaged ceramics were insensitive to strain rate once the damage level exceeded a critical level [16]. Recent mesoscale simulations of shock loading in a pressure-less

sintered 88% and a hot-pressed 99% alumina showed that HEL was determined by only plasticity within the grains and no tensile stress was created within the alumina grains even around inhomogeneities [17]. Further work in the same direction with the same materials led to the hypothesis that HEL corresponds to a condition at which damaged zones might join, interact and subsequently lead to failure of alumina [1]. The concept that HEL is a consequence of grain localized plasticity, got further credence from recent shock recovery work on high purity, fine grain alumina where presence of intergranular plasticity was confirmed by scanning electron microscopy (SEM), transmission electron microscopy (TEM) and high resolution electron microscopy (HREM) techniques [2] and also from recent molecular dynamics simulation of hypervelocity impact on the (0001) surface of α-alumina [18, 19]. It has been suggested further that in tensile loading, the lower strength glass/porous matrix will fail more easily than pure alumina grains and grain boundaries will be the favoured routes down which these fractures might extend [2]. Recent soft recovery plate impact experiments [20] in high purity fine grain alumina determined micro and macro deformation and damage mechanism maps relating the experimentally measured global mechanical response to the nature of concurrent deformation and damage generated at varying length scales under shock wave loading. The purpose of present work was to study the shock deformation behaviour of a coarse grain alumina through shock recovery experiments conducted at a shock pressure level much higher than the HEL and to characterize the micromechanical properties of the alumina fragments recovered after the shock experiments by the nanoindentation technique.

Materials and methods

99.9% dense alumina discs (diameter ~48 and thickness ~2.5 mm), 99.99% pure α-alumina powder (Morimura Bros. Inc., Tokyo, Japan) pressureless sintered at 1310 °C were used in the present experiments. The average grain size was determined using polished and thermally etched samples with an image analyzer (Leica, Q 500 MC, UK).

Two types of experiments were conducted in the present work. The first one was a typical shock experiment where alumina ceramic target was shock loaded in a 63 mm bore size Gas Gun [22, 23] (Fig. 1a) in symmetric configuration (Fig. 1b) with an alumina flyer plate at 0.41 km s^{-1} to measure the Hugoniot elastic limit (HEL) and the shock pressure profile during shock compression and velocity history of free surface after unloading from peak shock pressure. The second one was a shock recovery experiment, in which the alumina ceramics were deliberately shocked to a pressure more than about three times the HEL and subsequently recovered for post-shock examinations. As shown in Fig. 1b, the target assembly for the symmetric configuration comprised of two identical alumina discs (diameter—48 mm, thickness—2.5 mm) glued using epoxy and fitted in a matching hole made on a Perspex disc (diameter—120 mm, thickness—5 mm). A piezo-resistive gauge placed at the interface between these two target plates recorded the shock pressure profile during shock compression and the velocity interferometer system for any reflector (VISAR) recorded the fringe shift due to the motion of free surface of the target plate upon the arrival of the shock at the free surface. The shock pressure profile was determined from the measured voltage profile across the active element of the gauge as:

$$P = \frac{1}{k}\frac{\Delta V}{V_0} \tag{1}$$

where P, ΔV, V_0 and k are shock pressure, increase in voltage, initial voltage and calibration constant (in our case it is 0.025/GPa). From the measured shock pressure profile the peak shock pressure (P_{max}) reached by the sample was determined. The particle velocity U_p in the sample was determined as ½ V_p, where V_p is the flyer velocity measured just before the impact with the target. The shock velocity U_s in the target was then estimated using measured peak shock pressure, particle velocity and initial density (ρ_0) of the sample in second jump condition as follows:

$$U_s = \frac{P_{max}}{\rho_0 U_p} \tag{2}$$

The free surface velocity history was derived from the fringe shift recorded using VISAR. The HEL and corresponding strain rate from this history was determined as follows [24, 25].

$$\text{HEL} = \frac{1}{2} U_H \rho_0 C_l \tag{3}$$

$$\dot{\varepsilon}_c = \frac{U_H}{2\Delta t_1}\frac{1}{C_l} \tag{4}$$

The dynamic yield strength (Y) from the HEL was deduced using the expression:

$$Y = \text{HEL}\frac{(1-2\nu)}{(1-\nu)} \tag{5}$$

Here, U_H is the free surface velocity at HEL, Δt_1 is the time taken for free surface to reach a velocity of U_H, C_l and ν correspond to longitudinal sound velocity and Poisson ratio, respectively.

Figure 1c shows the schematic of recovery fixture (a special SS304 capsule) holding the brittle alumina sample. The details are discussed elsewhere [22]. This fixture was mounted on a target ring in the target chamber of the gun and impacted by a SS304 flyer plate (diameter—57 mm,

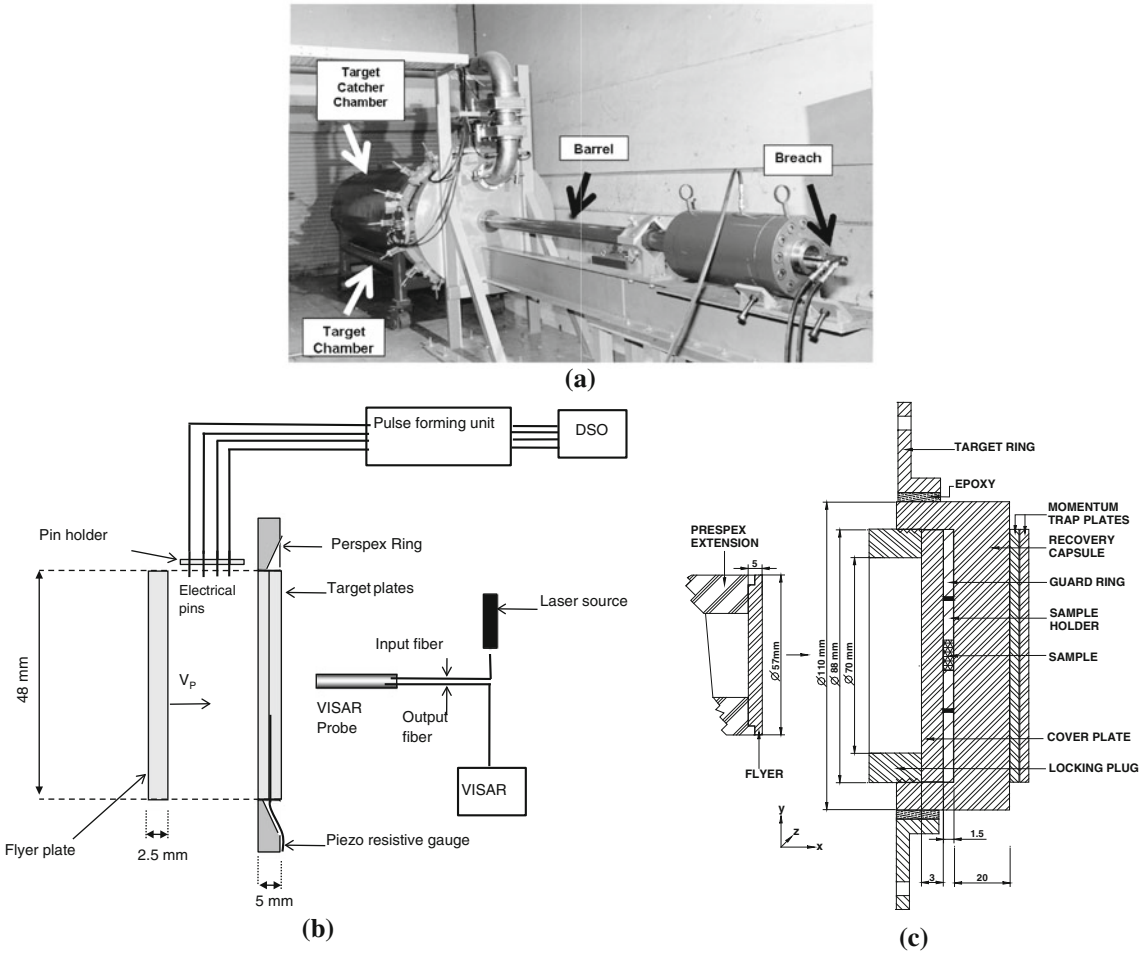

Fig. 1 (**a**) Photograph of the arrangements of gas gun shock experiment. Schematic of (**b**) experimental setup for HEL measurement and (**c**) assembled recovery fixture used for shock recovery experiment also showing the location of the test sample

thickness—5 mm) accelerated to a velocity of 0.33 km s^{-1}. The sample fitted in the central hole of SS304 ring and covered by SS304 plate at one side and by fixture wall at other side, reached the peak pressure through reverberations. The sample after shock compression was retrieved by careful machining of the recovery fixture.

The phase composition, crystallite size, microstrain etc. of the as-received powder, the as-sintered disc and the shock recovered alumina samples were evaluated by analyzing the X-ray diffraction (monochromatic Cu $K_{\alpha 1}$ radiation, 35 mA, 45 kV, Philips PW1710, The Netherlands) data by Rietveld technique using X'pert high score plus software (PAnalytical). The deformation behaviour of the as-received and the shock recovered alumina sample was studied by the nanoindentation technique utilizing the Oliver and Pharr (O–P) model [26], from nanohardness (H) and Young's modulus (E) data obtained at 10–1000 mN with at least five numbers of 5×5 array from a commercial machine (depth resolution—1 nm, force resolution—0.2 μN, DIN 50359-1 standard, Fischerscope H100-XYp; Fischer, Switzerland). The characterizations of deformation features in and around the nanoindents as well as of the alumina fragments obtained from the shock recovery experiments were carried out using SEM (s430i, Leo, UK), field emission scanning electron microscopy (FE-SEM) (Supra VP35 Carl Zeiss, Germany) and TEM (Tecnai, G2 30, S-Twin, 300 kV, FEI, The Netherlands, LaB_6 Filament, Line Resolution 0.14 nm, Point Resolution 0.2 nm).

Results and discussions

Structural characterization of alumina

The typical XRD data (Fig. 2a) of the sintered alumina discs matched with the standard data of α-alumina (JCPDS-43-1484). The microstructure of the alumina sample used

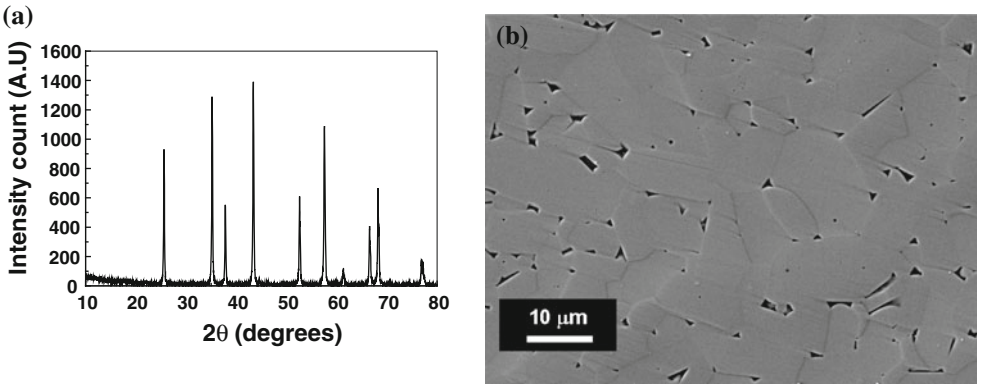

Fig. 2 **a** XRD pattern and **b** SEM photomicrograph of sintered alumina

in the present work is shown in Fig. 2b. The microstructure was very dense with only pores at triple grain junctions but the grain size distribution was a bit heterogeneous. The average grain size as measured by the linear intercept method using an image analyzer was $\sim(10.1 \pm 0.23\ \mu m)$.

HEL determination and shock recovery experiments

Various parameters measured or derived from measured quantities for the target material are listed in Table 1. The impact velocity for the first experiment designed to determine the HEL was measured to be 0.41 km s^{-1} by using electrical pin shorting technique [15]. A typical corresponding voltage profile recorded by the piezo resistive gauge is shown in Fig. 3a. However, such data should be treated with some amount of cautionary remark. As such, the gauge record in Fig. 3a shows an elastic wave rise time of around 100 ns which is unusually slow for armour ceramic. For the present material having density 99.9% of theoretical, one would have expected an elastic wave rise time of the order of sub ns, which did not happen. This aspect has been dealt later in details. However, such an experimental observation might indicate that there was a ramping in the pulse with impedance mismatches or there could be some slight misalignment in the experiment which could have taken the target out of the strict paradigm of perfect 1D strain condition at the continuum. The ΔV_{max} and V_0 determined from this record were 493 and 2,120 mV, respectively. The peak shock pressure determined using these values in Eq. 1 was $\sim$9.3 GPa. As is clear from the data presented in Fig. 3a, a break in the profile occurred at $\sim$100 mV which was due to elastic to plastic transition in the material and the compressive stress corresponding to this, defined as the HEL, was determined to be 1.89 GPa.

Table 1 Various parameters measured or derived from measured quantities for target

Parameters	Values
ν	0.27
ρ_0 (g cc^{-1})	3.978
E (GPa)	400
C_l (km s^{-1})	10.03
V_p (km s^{-1})	0.41
P_{max} (GPa)	9.3
HEL (GPa)	
Using shock pressure profile	1.89
Using free surface velocity history	1.91
Y (GPa)	1.2
U_s (km s^{-1})	11.43
Compression ratio (ρ/ρ_0)	1.018

Figure 3b shows the VISAR output along with the free surface velocity history derived from it. As it is clear from the data presented in Fig. 3b the measured peak free surface velocity was $\sim$0.39 km s^{-1} which, as expected, is close to the measured impact velocity of 0.41 km s^{-1}. This data matched favourably with that reported by others [15]. Further, there was a break in the free surface velocity profile at $\sim$96 m s^{-1} (U_H), Fig. 3c, which corresponds to HEL of the alumina sample. The value of C_l required for determination of HEL is taken to be 10.04 km s^{-1} derived from the Young's modulus (E) of 400 GPa measured by the nano-indentation technique and density of 3.978 g cc^{-1}. The value of HEL and corresponding strain rate determined using Eqs. 3 and 4 were 1.91 GPa and 4×10^4 s^{-1}. Thus, the value of HEL determined using VISAR was close to that measured from the shock pressure profile. The dynamic yield strength of the alumina sample determined using $\nu = 0.27$ available from literature in Eq. 5 is 1.2 GPa.

The HEL value of the present alumina ceramics was a little bit on the lower side, presumably due to its higher grain size, as is evident from a plot (Fig. 3d) of literature data on HEL of alumina [6, 14, 27] and the data from present work as a function of grain size. The data were for alumina with residual porosity in a comparatively narrow band of $0.5 \leq P \leq 3.8\%$, as suggested by Murray et al. [3], to avoid the scatter in data and also to avoid the strong, masking influence that porosity may have on HEL of alumina ceramics [6, 14]. The linear fit with a goodness of fit

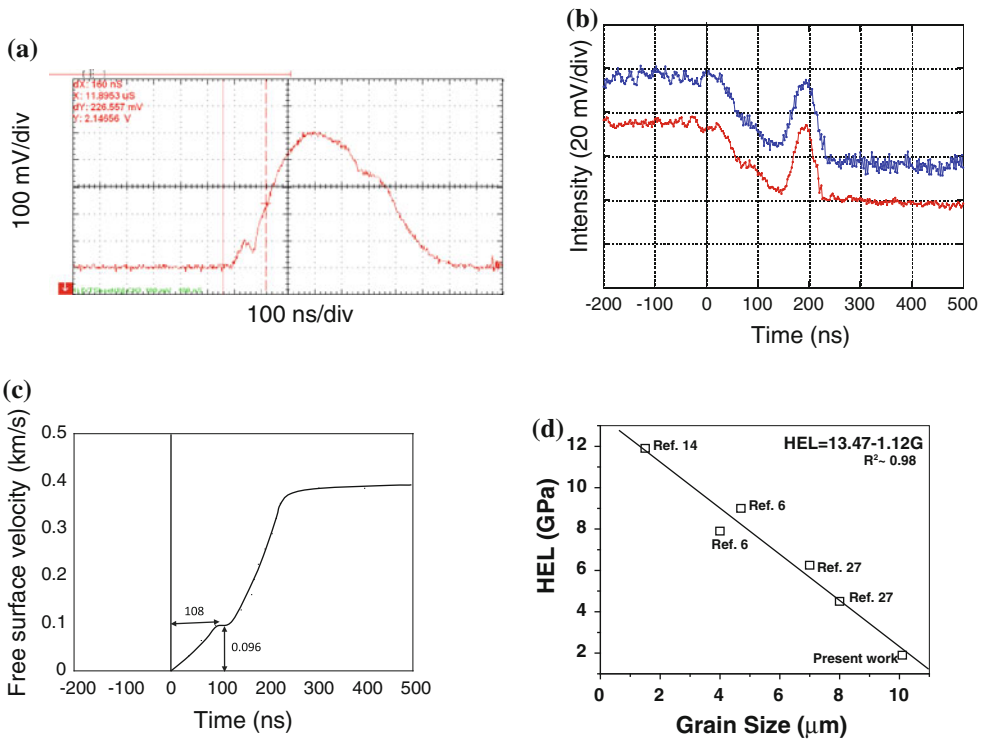

Fig. 3 (**a**) Voltage profile recorded from piezo resistive gauge in shock wave experiment, (**b**) VISAR output, (**c**) corresponding free surface velocity profile derived from output and (**d**) plot of literature data on HEL of alumina [6, 14, 27] and the data from present work as a function of grain size

coefficient of 0.98 appears reasonable, although purely empirical in nature. The resultant relationship was:

$$\mathrm{HEL} = 13.47 - 1.12G \tag{6}$$

where G represents the grain size of alumina. Equation 6 predicts the HEL of the present alumina ceramics as about 2.2 GPa which matched reasonably with the experimentally measured data of $\sim$1.9 GPa. The predicted trend was a decrease of HEL with an increase in grain size. This behaviour is expected because static compressive strength of alumina also decreases with the grain size [28]. However, the nature of dependence of HEL and/or compressive strength on grain size is yet to be unequivocally established. For instance, Knudsen [29] and Griffith [30] have proposed the following relationships:

$$\sigma = \beta G^{-n} \tag{7}$$

$$\sigma = \delta\left(E\gamma a^{-1}\right)^{0.5} \tag{8}$$

between static strength σ and grain size (G) of brittle materials. In Eqs. 7 and 8, σ is the strength of material, n is the pre-exponential factor, E is the Young's modulus, γ is the surface energy and "a" is the mean flaw size. The term β is an empirical constant. Similarly, the term δ is a factor that takes care of the crack geometry. On the other hand the well-known Petch relationship is given by Petch [31],

$$\sigma = \kappa + \phi G^{-0.5} \tag{9}$$

In Eq. 9 κ and ϕ are again constants to be determined by empirical data fitting technique. In the limiting situation of primary crack size equal to a grain size, and assuming $\kappa = 0$, would reduce Eq. 9 to Eq. 8, the Griffith relationship. Similarly, assuming "n" value of 0.5 would reduce Eq. 7 to Eq. 8. It is interesting to note that an attempt to fit the data used in Fig. 3d to the Knudsen relationship (Eq. 8) would yield a predicted HEL almost twice as high (e.g. 3.4 GPa) as the experimentally measured data. An even higher value (e.g. 4.24 GPa) is predicted if we attempt to fit the same data as mentioned above (Fig. 3d) to the Petch relationship (Eq. 9). The goodness of fit coefficients were also much poorer (e.g. 0.7 for Eq. 8 and 0.8 for Eq. 9) than that (e.g. 0.98) obtained with the empirical linear relationship (Eq. 6). This information would apparently suggest that these models [29, 30] may have some limitations when applied to high strain rate data of coarse grain alumina. However, this is not totally surprising because they were mainly developed with a focus on strength of brittle materials with flaws in a state of localized tension. In the present experiments with a plate impact configuration in symmetric mode the coarse alumina is expected to experience, on the contrary, a significant amount of hydrostatic stress. This would lead to a situation whereby the flaws are most likely to be surrounded by both compressive as well as shear stress fields. The attempt to fit the Petch relationship yielded a non-zero intercept (e.g. 1.14) for the present data (Fig. 3d). This information indicated a situation where the strength of alumina is controlled rather by micro-plastic events than by the usual critical size flaws [28]. Based on this HEL data, the shock

recovery experiments were subsequently conducted at 6.5 GPa, i.e. at a pressure of about 3.2 times the HEL value. These experiments were deliberately done to understand the deformation and fracture mechanisms of the present alumina ceramics by shock loading at high strain rate, e.g. $\sim 10^4$ s^{-1} under a pressure reasonably higher than the HEL. Then, as detailed in the section on "Experimental Materials and Methods", a dedicated target catcher chamber was used to recover the alumina sample after the shock experiment. The fragments of alumina recovered after these experiments were very tiny at about 0.04–0.05 by 0.03–0.04 by 0.02–0.03 mm in size. Along with these fragments, a certain amount of almost powdered alumina sample was also recovered.

It may be noted that the loading history in above-mentioned two types of experiments are not exactly identical. In case of recovery experiments the aim was to perform post shock analysis of the sample which required the safe retrieval of the shocked sample. The recovery of the sample after shock loading was quite difficult, especially in case of brittle samples; hence it was essential to enclose the sample in a suitably designed recovery fixture. It should be admitted that although, attempts were made using momentum trap plates at the rear surface of the fixture and guard ring around the sample holding plate such that the effects of the longitudinal and lateral release waves on the sample gets mitigated but it was not possible to completely avoid this. Therefore, possibilities do exist that the recovery fixture did not trap all the lateral or longitudinal momentum from the impact pulse which will result in considerable loading out of the assumed one-dimensional strain period. Further there might have been impedance mismatch between the confining metal plates and the target which may be significant. A cautionary note should therefore be borne in mind that these features may affect the state of the recovered material and might as well imply that assumptions about the loading history may not be strictly correct. Nevertheless, the subsequent detailed X-ray diffraction, nanoindentation and microscopic data presented below do provide valuable qualitative picture about shock deformation of brittle solids in general, and of coarse grain alumina in particular. The release waves were operative in first type of experiments also but maximum possible care was taken to perform the measurements before the uniaxial strain condition gets significantly distorted.

XRD of shocked alumina

The XRD data of both as-prepared, sintered polycrystalline alumina discs and alumina fragments recovered after the 6.5 GPa shock experiment were taken and the data for the main intense peaks (113) were compared with the standard.

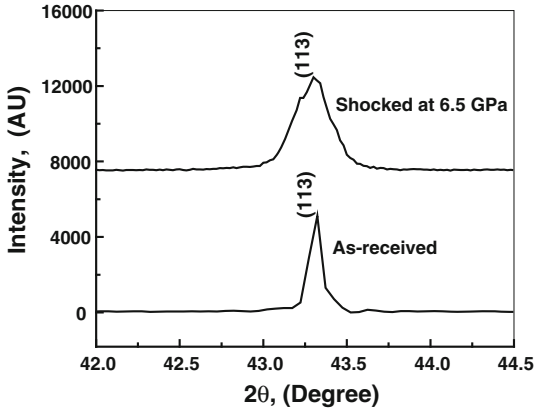

Fig. 4 XRD pattern of both sintered and shocked alumina

Table 2 The size-strain data of alumina under different conditions

	Size-strain of alumina	
	Size (nm)	Strain (%)
As-received alumina powder	58.51	0.245
As-prepared, sintered polycrystalline alumina discs	296.26	0.0843
Alumina fragments recovered after the 6.5 GPa shock experiment	127.21	0.168

It was found that the major peaks of alumina fragments recovered after the 6.5 GPa shock experiment had a shifted position (Fig. 4) in comparison to that of the as-sintered alumina disc suggesting possibly the presence of a strained lattice. Results from additional XRD studies [32, 33] showed that the average crystallite size in the alumina fragments recovered after the 6.5 GPa shock experiment decreased by $\sim$57% from its initial value of 296.26 nm (Table 2). In addition, there was a corresponding increase in the average microstrain percentage from $\sim$8.43% in as-sintered alumina to $\sim$16.8% in the alumina fragments, thereby confirming the presence of a strained lattice, as suggested from the data (Fig. 4), and as also observed by others [6].

Nanoindentation behaviour of shocked and un-shocked alumina

The data on nanohardness (H) and Young's modulus (E) behaviour of the as-prepared, sintered polycrystalline alumina discs and the alumina fragments recovered after the 6.5 GPa shock experiment are presented as a function of load (10–1000 mN) in Fig. 5a and b. The most important observation from the nanoindentation experiments was that the average values of (H) and (E) of the alumina fragments recovered after the 6.5 GPa shock experiment were reduced by about 15% (Fig. 5a) and 27% (Fig. 5b),

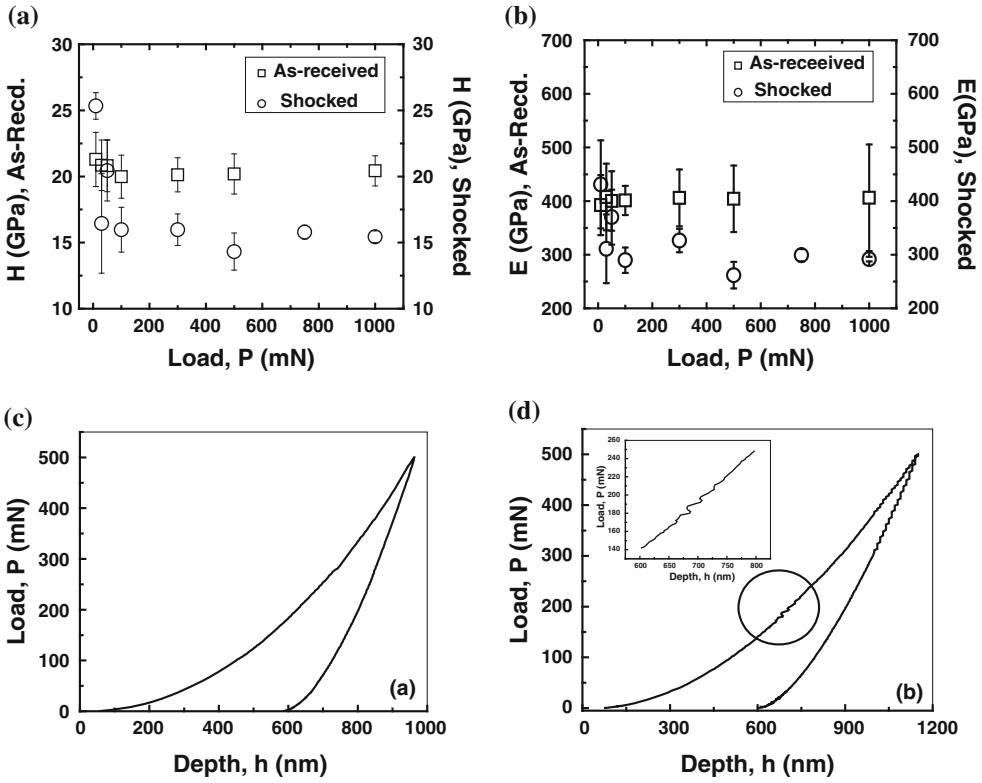

Fig. 5 Variation of (**a**) hardness, (**b**) elastic modulus as a function of load for both sintered and shocked alumina. Load–depth plots of both (**c**) sintered and (**d**) shocked alumina

respectively, as compared to those of the as-prepared, sintered polycrystalline alumina discs. This decrease in nanohardness and Young's modulus data was possibly linked to the high amount of strain present (Table 2) in the alumina fragments recovered after the 6.5 GPa shock experiment and/or presence of microcracks in them. The corresponding typical load (P) versus depth (h) plots Fig. 5c and d, showed that for a given constant peak load, e.g. 500 mN, the P–h plot was smooth for as-received alumina and a pop-in appeared (as shown in inset of Fig. 5d) in the P–h plot of shocked alumina suggesting strongly the presence of microcracks as was indeed observed around a typical nanoindent impression (Fig. 6a).

Scanning electron microscopy of shocked alumina

Several interesting characteristic features were noted on the fracture surface of alumina fragments recovered from the sintered polycrystalline alumina discs after the 6.5 GPa shock experiments (Fig. 6b–d). Apart from the characteristic presence of transgranular fracture regions (marked as "T" in Fig. 6b), there were many regions of intergranular fracture, grain boundary microcracking (marked with short arrowheads as "M"), zones of localized cleavage fracture and/or plastic deformation (marked with broken, longer arrowheads as "P"), as well as regions of macrocrack formation (marked with black arrowhead). These characteristic features were absent in the typical brittle fracture surface of as-sintered polycrystalline alumina discs (shown as inset of Fig. 6b). Further details of the fracture process are shown in Fig. 6c and d. It may be noted that the failure process at individual grains were quite complex and actually involved both in-plane and out-of-plane fracture propagation, Fig. 6c. There were several layers inside a single grain which appeared as twisted and subsequently cleaved along favourably oriented planes leading to several regions of shear-induced slip band formation (marked as "S" in Fig. 6c), localized regions of extensive grain boundary micro-fracture (marked as "MF" with a hollow, blue arrowhead) and intra-granular crack propagation (marked as "L" with a hollow, red arrowhead).

These features would strongly suggest the presence of a shear stress component to be actively participating in the failure initiation, incubation and its subsequent propagation. Inside the broken parts of some single grains also there were two distinct features noted, one was the regions of stepped micro-fracture/micro-cleavage zone with step heights much less than a micron (marked as "MF" with a hollow arrowhead) and the other was an adjacent extensive area of slip/deformation band formation (marked as "SB" with a hollow arrowhead), Fig. 6d. The width of the individual lines inside the deformation band were about 30–40 nm, suggesting thereby the importance of the submicroscopic and/or nano-scale regime of microstructure in determining the response of shock loaded alumina. In addition, this observation again strongly suggests a major

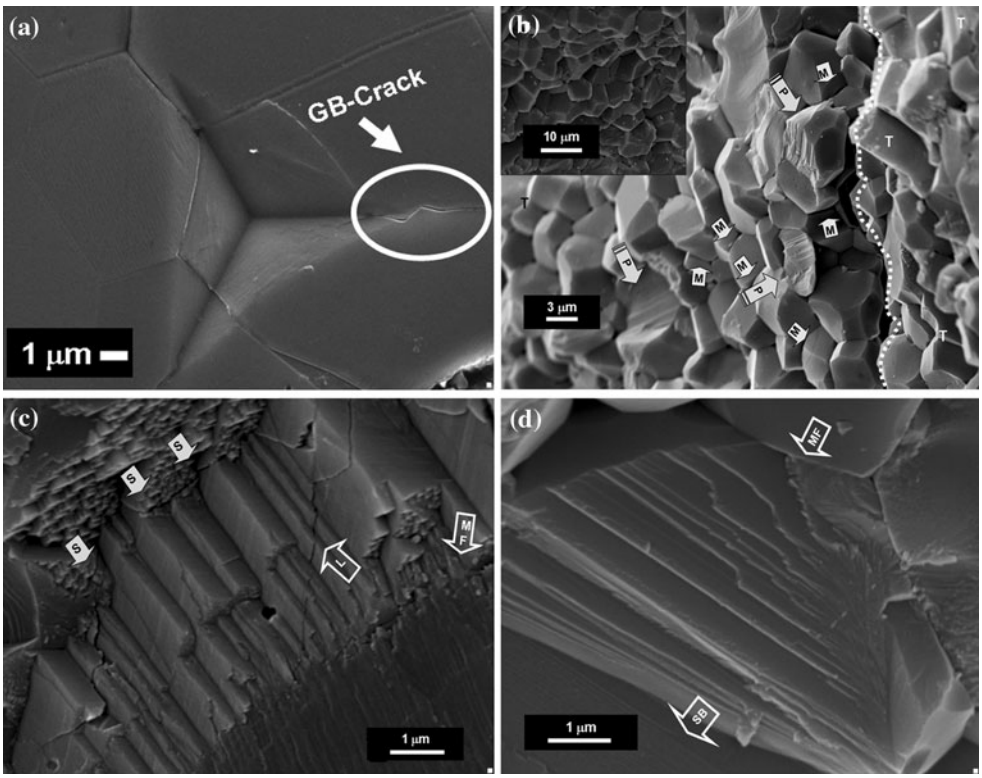

Fig. 6 SEM photomicrograph of the (**a**) Berkovich indentation, (**b**) fracture surface of shocked and sintered alumina (inset), fracture surface of shocked alumina showing step fracture (**c**) fracture surface of shocked alumina showing micro-fracture/micro-cleavage and (**d**) slip/deformation band

role being played by the shear dominated failure processes. Such dominance appeared to be active during both out-of-plane (Fig. 6c) and in-plane (Fig. 6d) propagation of the shock wave through the alumina sample.

Field-emission scanning electron microscopy of shocked alumina

FE-SEM-based evidences showed the presence of various distinctive features, e.g. grain boundary cracking and micro fracture, Fig. 7a, formation of intra-granular deformation band and inter-granular regions of micro-cleavage due to local twisting and/or out of plane damage propagation, Fig. 7b, deformation band of width of about 10–40 nm, Fig. 7c and their orientation in mutually perpendicular directions (indicated by arrows), Fig. 7d. Additional features included grain localized cleavage and transgranular fracture, Fig. 7e, grain boundary microcracks originating at multiple locations depending on the favourable spatial orientation of the grain, Fig. 7f and micro-cleavage region of sheared out broken grain with cleaved plates of 10–40 nm thickness, Fig. 7g. These damages were possibly caused by shear stress-induced damage propagation in planes mutually perpendicular to the direction of shock propagation. Further, debris of size ranging from about 5 to 50 nm was amply present in the cleaved region. This information again highlights that damage initiation can really begin at sub-microscopic regions of microstructure and can indeed be grain-localized as postulated as well as experimentally observed by other researchers in the case of high purity fine grain alumina [1, 2, 17] and other ceramics [34, 35].

Transmission electron microscopy of shocked alumina

TEM observations showed remarkable amount of dislocation entanglement at triple point in the alumina fragments recovered after 6.5 GPa shock experiment (Fig. 8a), stacking fault in single grain, Fig. 8b, grain boundary microcrack formation, Fig. 8c, fractured grain, Fig. 8d and a region of very fine (5–50 nm) agglomeration of adhered debris smeared on the fractured grain, Fig. 8e. Similar observations have been reported also by others [11, 12, 14]. Further, the TEM observations compliment and corroborate with the SEM observations (Fig. 7f, g) mentioned above. This debris must have been produced by a process of continued fragmentation and repeated comminution at a localized scale.

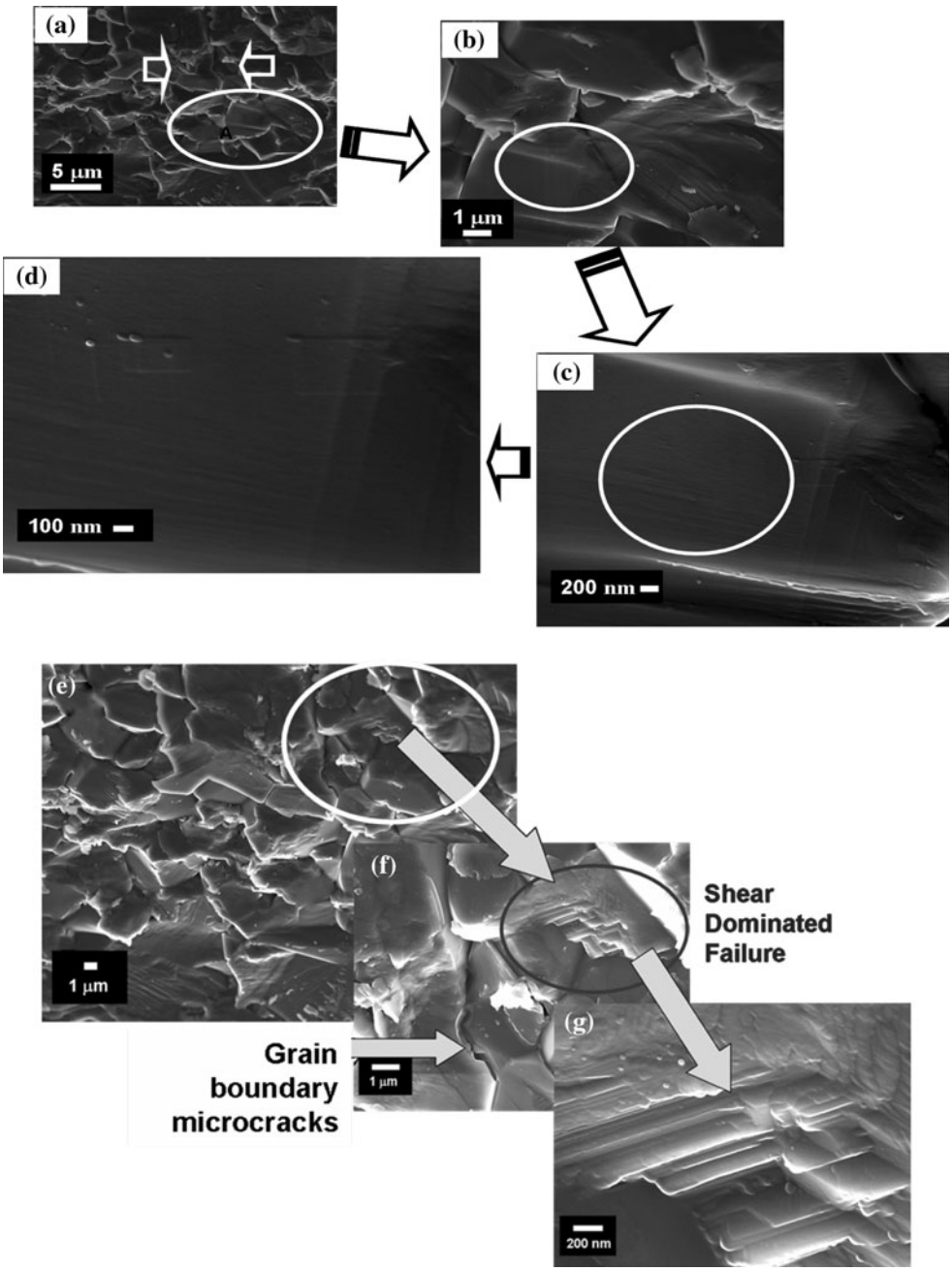

Fig. 7 FE-SEM photomicrograph of the shocked alumina showing **a** grain boundary cracking and micro fracture, **b** formation of intra-granular and inter-granular shear band, **c** intra-granular shear band and **d** intra-granular shear band at higher magnification. **e** Grain boundary microcracks and shear dominated failure, **f** intra-granular shear band and **g** intra-granular shear band at higher magnification

Discussions

The present shock recovery experiments were deliberately conducted at a shock pressure about three times the experimentally measured HEL of the 10 μm grain size alumina. When a ceramic is loaded by high-intensity shocks from the plate impact, many cracks do form and propagate/interact simultaneously. The present SEM- and FE-SEM-based evidences (Figs. 6, 7) do suggest that this can happen, not only in-plane but also out-of-plane in the 3-D microstructure of alumina. Simultaneously, it can also happen in multiple planes in a given microstructural element or in an ensemble of microstructural elements depending on its local orientation with respect to the direction of shock wave propagation (Figs. 6, 7, 8). Simultaneous repetition of many such unit steps within a few ns time interval creates a comminuted zone of highly pulverized, crushed ceramic debris ahead and around the flyer plate which also gets eroded in the process. That is why the SEM- and FE-SEM-based photomicrographs of the alumina debris collected after shock at 6.5 GPa depict presence of a variety of characteristic features, e.g. showing micro-fracture/micro-cleavage and slip/deformation band formation, intra-granular and inter-granular shear

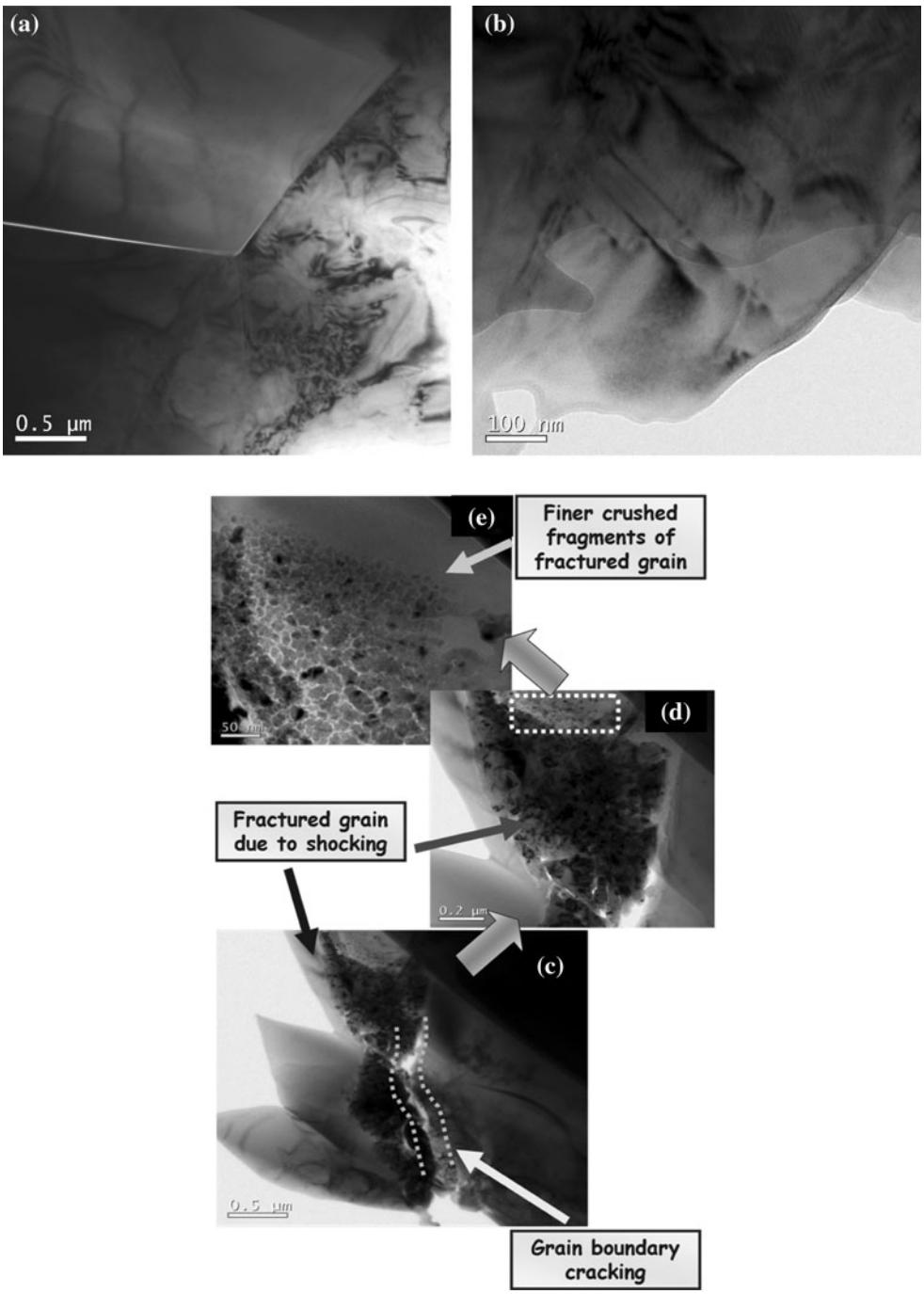

Fig. 8 Dislocation entanglement at (**a**) triple point (**b**) stacking fault in single grain (**c**) grain boundary microcrack (**d**) fractured grain adjacent to (**c**) along with intra-granular cracks and agglomerated debris and (**e**) higher magnification view of (**d**) showing a region of very fine (5–50 nm), crushed agglomeration of adhered debris in the alumina fragments recovered after 6.5 GPa shock experiment

band, shear dominated failure and grain boundary micro-cracking. Similar observations were reported for a fine grain high purity alumina by Chen et al. [2]. It is well known that both plasticity and fracture are viable operative mechanisms for intense shear stress dominated inelastic deformation under compressive loading. Evidences from the present experiments show presence of both intense plastic deformation and micro-fracture events in the alumina debris. Recent literature data on high purity alumina does really indicate that HEL was determined by only plasticity within the grains [1, 2, 14, 17–19]. However, the relative amount of dominance from plasticity based processes and fracture-based processes under the range of actually tri-axial impulse loading condition experienced by the current alumina sample is yet to be unequivocally ascertained. Chen et al. [2] has suggested that in high purity fine grain alumina generation of deformation twins in the shock-loaded alumina may provide an energetically more favourable path, for cleavage cracking, and thereby a change in the fracture mode from intergranular cleavage

failure behaviour in experiments conducted below the HEL to transgranular cleavage failure behaviour in experiments conducted above HEL. No twins were, however, observed in the SEM, FE-SEM or TEM examinations of the debris from 6.5 GPa shock experiments conducted on the present, high purity but coarse grain alumina. It has been further suggested [2] that the cleavage along the twin boundaries is caused by the deviatoric stresses applied to the twin bands during unloading and the relatively weak chemical bonding at the non-relaxed twinning interfaces.

As, the overall loading is compressive, microcracks are nucleated at pre-existing flaws (Fig. 6b). However, local tensile stress field would be needed to propagate such microcracks. It is plausible to argue that upon compression, there can be slippage on the microstructural scale, processing induced intrinsic, pre-existent flaws. Such slippages produce tensile stresses at the end-points of the flaw. These tensile stresses can then trigger the formation of cracks. Voids and inclusions, for example, also can act as flaws and play as a precursor site for failure initiation. Micrographs presented in Figs. 6 and 7 support this picture.

Microcracks are also possible due to piled up dislocations. Applied stress can generate dislocations through Frank-Read or Stroh sources. Such dislocations may be stopped and subsequently piled up along their slip planes at local obstacles such as the grain boundaries. Transmission electron microscopic evidence (Fig. 8a) indeed show a huge localized entanglement of dislocations at the grain boundary triple point in the alumina fragments recovered after 6.5 GPa shock experiment. Due to the applied shock pressure when a high shear stress is developed at the leading dislocation of a pile up of dislocations, e.g. as in Fig. 8a, the only way to relax the stress is by nucleation of a microcrack, Fig. 8c. As these microcracks coalesce along grain boundaries, it induces intergranular fracture, Fig. 8d. Additional TEM based evidences (Fig. 8e) showed an agglomeration of very fine (5–50 nm) debris still adhered and smeared onto the broken grain which might have been produced only by a process of continued fragmentation and repeated comminution at a localized scale, [13]. Further support to such a picture is also provided by the experimental observations of Lankford et al. [36] on the role of plasticity as a limiting factor in the compressive failure of AlN and alumina samples of various grades, e.g. AD 995, JSI, JSII. Of these last two alumina samples, it was noted that JSI had a finer grain size thereby requiring higher magnitude of critical resolved shear stress to be able to operate on a suitably oriented slip plane. As a result, this relatively purer alumina could show the ability to reach its plastic yielding limit under pure uniaxial compression. On the other hand, it was noted that JSII alumina had a larger grain size and some residual grain boundary porosity thereby requiring lower magnitude of critical resolved shear stress to be able to operate on a suitably oriented slip plane. As a result, this sample showed dislocation pileups to reach criticality which induced generation of microcracks. Nevertheless, JSII alumina also exhibited microplasticity under high strain rate condition. This situation is similar to the observations of the present work. According to these authors [36], the critical value of resolved shear stress (τ_{crk}) on an operable slip plane from which a microcrack will nucleate is expressed by the following relationship:

$$\tau_{crk} = \left\{ \frac{\pi \gamma \Gamma f(\phi)}{2(1-\nu)d} \right\}^{\frac{1}{2}} \tag{10}$$

In Eq. 10, γ is the surface energy associated with the crack, Γ is the shear modulus, f is a geometrical function of ϕ, ν is Poisson's ratio, and d is the dislocation pile-up length. In turn, d is related to the grain size G of the sample. It should be noted that here the term "ϕ" represents the angle subtended by the suitably oriented slip plane and the projected crack. Their experimental observation showed that γ could be associated with a variety of microcrack types which could be nucleated, e.g. surface energy of preferential intercrystalline cleavage (c.f. Fig. 15), surface energy of slip plane cleavage (c.f. Fig. 16) and the grain boundary surface energy (c.f. Figs. 17a, 18b, 21a). It has been suggested also by these researchers that the observed mode of cracking would depend on the combination of slip band, grain boundary and the relative orientation of the potential cleavage plane. Even without rendering to detailed calculation which would require an exact formulation of $f(\phi)$, that is yet to be precisely known; it may therefore be qualitatively argued that the dislocation pile up length "d" of the present alumina sample would be on the higher side as it had a comparatively larger grain size, e.g. ~ 10 μm, and consequently, a lower magnitude of critical shear stress would be necessary to nucleate a microcrack at the head of the dislocation pileup from a favourably oriented slip plane.

The critical shear stress (τ_c) for the formation of stacking faults in perfect alumina crystals can be roughly estimated by only considering the relaxed energy γ_{SF} of stacking fault using the following equation [2],

$$\tau_c = \frac{\gamma_{SF}}{b} \tag{11}$$

where b stands for the Burger's vector. Assuming a typical value of $b \sim 0.5$ nm and $\gamma_{SF} = 1.2$–$2\ \mathrm{Jm}^{-2}$ following [37], $\tau_c = 2.4$–4 GPa which was much lesser than the applied shock pressure (6.5 GPa). Therefore, it can provide the shear stress necessary for formation of stacking fault, Fig. 8b. The estimated values of the critical shear stress also matched favourably with those (5–8 GPa) reported for alumina [2]. Similarly, the critical strain rate for sensitivity of strength to strain rate can be estimated as [38]:

$$\frac{d\varepsilon_c}{dt} = \frac{\sigma_c}{Et_c} \quad (12)$$

where $\frac{d\varepsilon_c}{dt}$ is the critical strain rate, σ_c is the quasi-static compressive strength, E is the Young's modulus and t_c is the time required for a crack to propagate across the sample thickness (2.5 mm). Putting σ_c conservatively as $\frac{H}{3}$, i.e. 6.67 GPa, $E = 400$ GPa, experimental value of $t_c \sim 1.64$ ms, $\frac{d\varepsilon_c}{dt}$ is $\sim 1.01 \times 10^4$ s^{-1} which matched with the experimentally measured data of 4×10^4 s^{-1}. Thus, the strength of alumina was expected to exhibit strain rate sensitivity. Lankford et al. [36] also noted from SHPB and flyer plate experiments on coarse grain alumina that compressive strength was strain rate sensitive, particularly at strain rates $\geq 10^2$ s^{-1}.

Model for the damage process

Numerous efforts have been made [39–53] to model the impact failure of brittle ceramics. The famous Johnson–Holmquist model [39] involved the strength of the intact and the comminuted material, the Rajendran–Grove model [42] assumed an existing distribution of microcracks that grow according to dynamic fracture mechanics, while the Espinosa [44, 47, 48] model considered nucleation and growth of penny-shaped microcracks in multiple-planes. The Grady model [13] considered the balance between time-dependent fracture and rate-dependent plasticity that allowed yield surfaces to vary with strain rate of the pulse delivered. The Bourne model [1, 17] established the role of grain localized plasticity in determining HEL. The Horii and Nemat-Nasser model [51] depicted that surface of a crack slide to form wing cracks under multiaxial compression when the resolved applied shear stress exceeds frictional stress due to normal forces on the crack surfaces. Recent micromechanical finite element modelling [52] indeed have showed that the onset of plastic deformation in alumina results from grain boundary shear (that must first occur in order for wing cracks to form) that creates a tensile stress acting on two neighbouring suitably oriented grain boundaries leading to mode I fracture thus forming a "micro-wing crack''. On continued loading, these tensile microcracks began to link eventually to form cracked microstructural scale slabs in the case with no lateral confinement, i.e. similar to the case of the present experimental conditions. Recent molecular dynamic simulation work [53] on dynamic failure of glass also supports this picture.

Based on the experimental data and SEM, FE-SEM and TEM based evidences presented above and existing literature [1, 13, 17, 39–53], we propose a qualitative model, Fig. 9, of the shock damage evolution process. Initially, prior to any shock exposure the as-sintered microstructure contains natural processing flaws, Fig. 9a (left part). However, following the first few moments after shock, due to the propagation of shock wave there can happen a significant increase in size and density of flaws in the alumina microstructure, Fig. 9a (right part) [54]. There can be micro-fracture due to tensile and compressive stresses, as well as local shearing and twisting of grains due to hydrostatic stress component, Fig. 9b [37, 44, 47, 48, 52, 53] which may be effective either independently or concurrently. As shown in Fig. 9b, this process can also give rise to grain boundary microcracks, which can act as further damage initiation points.

As the shock wave propagation continues inside alumina, there may be shear fracture initiation at a single plane in a favourably oriented grain, Fig. 9c (i) thereby breaking it into two pieces, Fig. 9c (i′). However, because of the actual presence of a multi-axial stress state shear fracture initiation can also occur at multiple planes [44, 47, 48] in a favourably oriented grain, Fig. 9c (ii), thus leading to formation of multiple fragments, Fig. 9c (ii′). Similarly, there may be twist fracture initiation at a single plane in a favourably oriented grain, Fig. 9c (iii), [55] thereby breaking it into two pieces, Fig. 9c (iii′). However, twist fracture initiation at multiple planes in a favourably oriented grain, Fig. 9c (iv), shall lead to formation of multiple broken pieces, Fig. 9c (iv′). These two processes can occur either independent to or concurrent with each other depending on which one is energetically more favourable. During the passage of the shock wave through the ceramic microstructure such unit events will many times repeat itself through a large multitude of individual grains and/or assembly of grains. As a result of these processes, multiple cracks will grow, coalesce and propagate very fast to cause fragmentation of the microstructure, as shown schematically in Fig. 9c (v). The combined effect of tensile and shear stresses on the fragmented and highly comminuted alumina, Fig. 9d (i), leave behind their markings in terms of a large number of microcracks (c), stacking faults (T), dislocations (D), shear deformation bands (SB) etc. as shown schematically in (Fig. 9d (ii). Thus, the qualitative model proposed here for alumina dynamically loaded to shock pressure value more than three times HEL supports the important role of multiple plane microfracture events [48] in determining the damage evolution of brittle materials.

Finally, based on the present SEM, FE-SEM and TEM based evidences, above discussions and keeping Gradys [13] shock compression profile of ceramics in view we propose in Fig. 10 a qualitative picture of the kinetics of shock damage process due to gas gun shock-induced impacts at shock pressure more than three times the HEL of the present alumina ceramic. We suggest that when a ceramic is loaded by high-intensity shocks at shock pressure

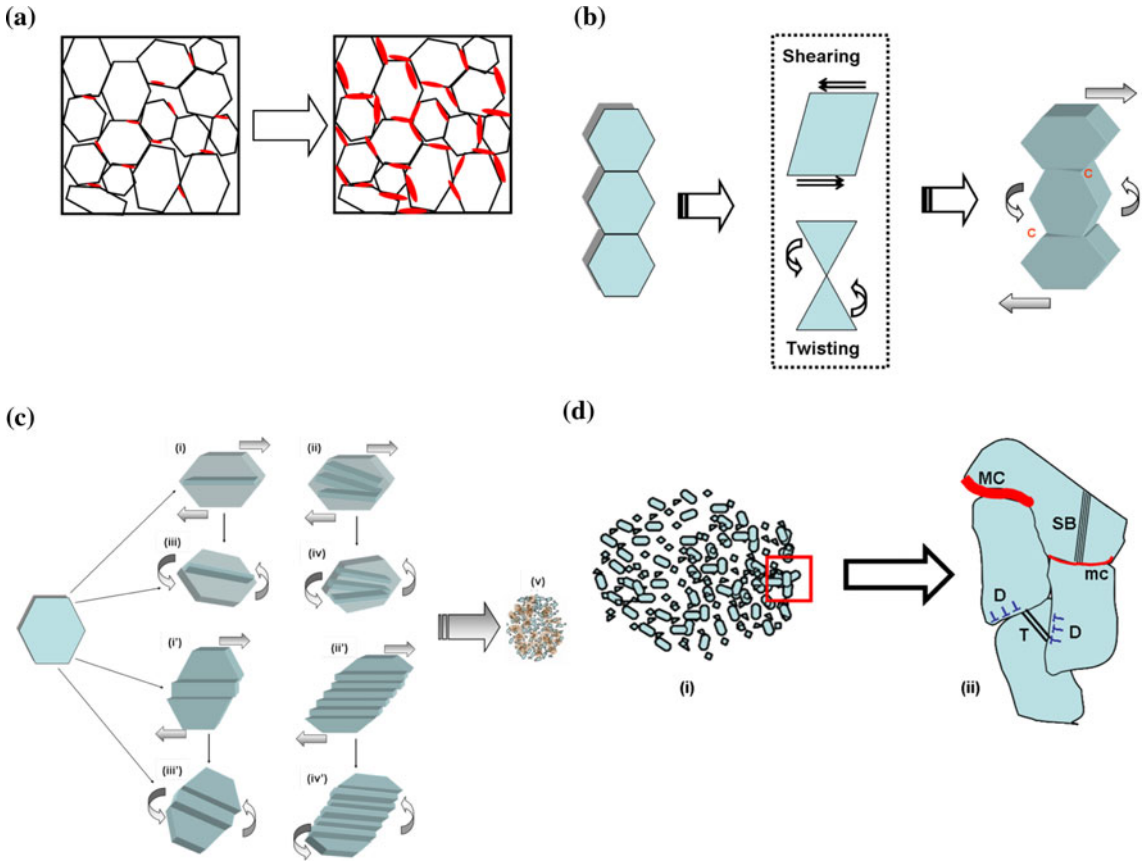

Fig. 9 Schematic model of the shock damage initiation process in alumina during the first few moments following shock (**a**) the as-sintered microstructure with natural processing flaws (*left*) and the increase in size and density of flaw (*right*), (**b**) inelastic damage evolution and incubation process in alumina following shock: the as-sintered microstructure (*left*), apart from micro-fracture due to tensile and compressive stresses, the grains can be locally sheared and twisted due to hydrostatic stress component (*middle*) and the locally deformed microstructure following the shear and twist (*right*), which could be effective either independently or concurrently. Notice that this process can also give rise to grain boundary microcracks (C) as further damage initiation points, (**c**) inelastic damage growth, coalescence and fragmentation process in alumina following shock (i) shear fracture initiation at a single plane in a favourably oriented grain, (i′) shear-fractured single grain, (ii) shear fracture initiation at multiple planes in a favourably oriented grain, (ii′) single grain after shear fracture at multiple planes, (iii) twist fracture initiation at a single plane in a favourably oriented grain, (iii′) single grain after twist fracture, (iv) twist fracture initiation at multiple planes in a favourably oriented grain, (iv′) single grain after twist fracture at multiple planes, (v) the process repeats itself at multiple grains. These cracks grow, coalesce and propagate very fast to cause fragmentation and (**d**) characteristic damage and deformation features in alumina fragments recovered after shock experiment at 6.5 GPa collected fragments (*left*) and presence of microcracks (MC), shear band (SB), dislocations (D), Stacking Faults (T) etc. (*right*)

levels much higher than the HEL through the appropriately conducted plate impact experiments, many cracks do form and propagate as well as interact simultaneously. The grain boundaries and other precursor weak spots can also act as initiation site for such defects. Following the elastic shock, the elastic damage processes are initiated first in alumina, as indicated in left portion of Fig. 10 and the corresponding inset marked as (a).

As the shock wave starts to pass through the material, inelastic shear-induced damages initiate and sub-critically grow; as indicated in the middle portion of Fig. 10 and the corresponding inset marked as (b). This is where the grain plasticity and the grain localized plastic deformation-induced processes come to play in a big way [1, 2, 17]. The nucleation can be initiated even at such small scales in the microstructure from a few tens to few hundreds of nanometres [18, 19, 53] up to a micron or so through formation of microcracks, stacking faults, dislocations, shear deformation bands etc. Further, it is plausible to argue that in the 3-D microstructure of the present alumina ceramic this can happen, not only in-plane but also out-of-plane. Simultaneously, due to multi-axial loading condition it can also occur in multiple planes in a given single grain and/or a collection of grains that is suitably oriented with respect to the direction of shock wave propagation.

Subsequently, as depicted in the right portion of Fig. 10 and the corresponding inset marked as (c), these inelastic damages grow to critical sizes, coalesce and propagate very

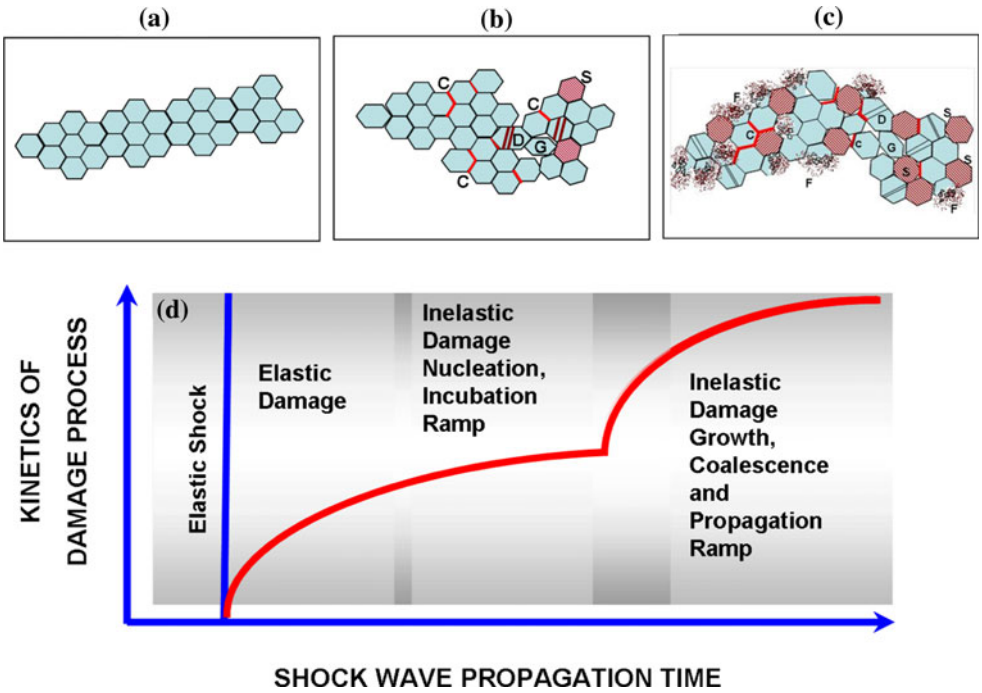

Fig. 10 Model of the kinetics of damage evolution process (see text for explanation)

rapidly [1, 2, 17–19, 53–55]. Ultimately, the simultaneous numerous repetition of such a unit process within a very short (few ms) time interval leads finally to fragmentation and comminution of the alumina ceramic.

In such processes it follows that the upper limit for crack velocity (v_c) is the Rayleigh wave speed (v_r) when the local stress intensity factor asymptotically reaches the critical value, i.e. fracture toughness (K_{Ic}). A suitable functional relationship between v_c and v_r can be written as:

$$v_c = f v_r \tag{13}$$

where the function f is such that f is <1 for all $v_c < v_r$ and $f = 1$ for $v_c = v_r$. The function f is given by a suitable function F such that,

$$f = \frac{1}{F} \tag{14}$$

where the function F involves the mode I stress intensity factor (K_I) and also the critical stress intensity factor under mode I loading (K_{Ic}). Now, following [54]:

$$F = [1 - e^{\alpha}(K_I^2 - K_{Ic}^2)] \tag{15}$$

In Eq. 15, α is a material parameter $\approx 1.2 \times 10^{-2}$ [54]. It may be noted that for all $K_I < K_{Ic}$, F is >1 and at $K_I = K_{Ic}$, F is =1, which automatically leads to the satisfaction of the boundary condition that for all $K_I < K_{Ic}$, $v_c < v_r$ and at $K_I = K_{Ic}$, $v_c = v_r$. Using literature data [56, 57] we estimate $v_r \sim 5.30$ km s^{-1}. Next using Eqs. 13 to 15, the variation of crack velocity as a function of the mode I quasi-static stress intensity factor is shown in Fig. 11a, where, the slopes in various regions were, e.g. along portions AB $\sim$ 0.10 km s^{-1} (MPa m$^{0.5}$)$^{-1}$, BC $\sim$ 0.83 km s^{-1} (MPa m$^{0.5}$)$^{-1}$, CD $\sim$ 3.56 km s^{-1} (MPa m$^{0.5}$)$^{-1}$, and finally, along DE $\sim$ 21.54 km s^{-1} (MPa m$^{0.5}$)$^{-1}$ which indicates that the maximum change in crack velocity occurs when the local stress intensity due to the applied shock pressure was in the range of about 96% of K_{Ic} to 100% of K_{Ic}. Sharp changes in gradient of the plot in Fig. 11a started to occur when the local stress intensity was $\geq$85% of K_{Ic}, e.g. from points C onwards. However, for the high velocity crack propagation scenario being considered here, the dynamic fracture toughness, K_{Id} would be a more appropriate material parameter than K_{Ic}. Accordingly, if we replace K_{Ic} by K_{Id} in Eq. 15, we have:

$$F = [1 - e^{\alpha}(K_I^2 - K_{Id}^2)] \tag{16}$$

Assuming a conservative estimate of K_{Id} as 1.3 times K_{Ic}, i.e. 4.15 MPa m$^{0.5}$, following the work of Suresh et al. [58], we can compute the variation in crack velocity as a function of the dynamic stress intensity factor as shown in Fig. 11b, where the slopes in various regions were, e.g. along portions AB $\sim$ 0.04 km s^{-1} (MPa m$^{0.5}$)$^{-1}$, BC $\sim$ 0.76 km s^{-1} (MPa m$^{0.5}$)$^{-1}$, CD $\sim$ 3.48 km s^{-1} (MPa m$^{0.5}$)$^{-1}$, and finally, along DE $\sim$ 23.25 km s^{-1} (MPa m$^{0.5}$)$^{-1}$ which indicates that the maximum change in crack velocity occurs when the local stress intensity due to the applied impact stress was in the range of about 97% of K_{Id} to 100% of K_{Id}. Here also sharp changes in gradient of the plot in Fig. 11b started to occur when the local stress intensity was $\geq$89% of K_{Id}, e.g. from points C onwards.

In both Fig. 11a and b there was a sharp change of slope from the point marked as "C" onwards, which thus defines

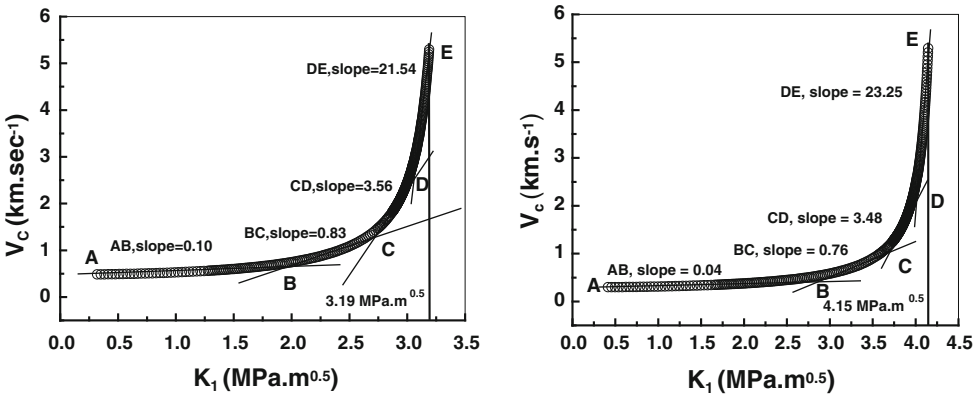

Fig. 11 Variation of crack velocity as a function of **a** static stress intensity factor and **b** dynamic stress intensity factor

these points as a characteristic "knee" beyond which a change in mechanism of crack growth must happen. The crack velocity v_c at C in Fig. 11a and b were 1.29 and 1.03 km s^{-1} with corresponding local stress intensities of 2.72 and 3.70 MPa $m^{0.5}$, respectively. These K_I values were about 85% of K_{Ic} and 89% of K_{Id}, respectively. This information also suggest that when the local stress intensity factor reaches beyond a "threshold" value it can initiate significant changes in crack growth mechanism which is also expected due to the continued evolution and accumulation of damage in the impacted microstructure [59].

However, these results should be taken with a cautionary remark that they provide a deliberately simplified picture, as a first-order estimate of the actual physical scenario. The reason for such caution stems from the fact that in reality the shock wave stresses the material in three dimensions. Thus, any estimate of the locally operative stress intensity factor should, in principle, consider crack growth under mode I, mode II and mode III loading whereas we have considered a limited possibility of mode I loading, *only in order* to develop a preliminary understanding which should be considered by no means as full and complete. Indeed it must be emphasized that there are excellent other models, e.g. [60, 61] which have considered in significant details the crack growth in brittle materials in mixed loading due to high strain rate impact events.

For instance, the micromechanical model proposed earlier by Ravichandran and Subhash [60, 61] considered a uniform distribution of non-interacting sliding microcracks from which tension cracks could nucleate and propagate from the tip of the sliding microcracks in the direction of maximum applied compression when the stress intensity factor reached its critical value. The model predicted that at an average critical strain rate of $\geq 1.1 \times 10^3$ s^{-1} transition to a strongly rate sensitive behaviour occurred for compressive strength of a brittle microcracking solid, e.g. AlN. This may imply that at strain rates higher than 1.1×10^3 s^{-1}, there must be a change in the crack growth mechanism to support and preserve the strain rate sensitivity of the compressive strength. As the strain rate in the present experiments was $\sim 4 \times 10^4$ s^{-1}, therefore a change in crack growth mechanism was expected to occur when the magnitude of the local stress intensity factor due to the applied shock pressure was close to the critical value of static (Fig. 11a) or dynamic stress intensity (Fig. 11b) factor, albeit even if, considered somewhat simplistically in *only mode I loading*. Thus, the first-order predictions of the present work were in tune with the predictions based on more rigorous micromechanical model [60].

Similarly, a recent micromechanical model by Huang and Subhash [61] for dynamic damage evolution in a brittle solid, e.g. basalt rock incorporated a unique combination of a material sensitive parameter, e.g. a Weibull distribution of existing, non-interacting microcracks, a kinematic parameter, i.e. the strain rate effect which assumes that the growth of microcracks occurred through "wing cracks" initiated from the pre-existing flaws and a brittle failure criterion which is considered to have had initiated when rate of damage (D) growth reached or exceeded a predetermined level. Numerical simulation results from this model also predicted a significant increase in strain rate sensitivity of failure strength at strain rate greater than $\sim 10^4$ s^{-1}; independent of whether the sample was under dynamic or static confinement pressure. It is therefore plausible to assume that a corresponding change in crack or damage growth mechanism must then happen in a commensurate fashion to sustain and preserve this strain rate sensitivity of failure strength. If this is true, then, at the strain rate of 4×10^4 s^{-1} utilized in the present experiments; a change in crack growth mechanism was expected to occur when the local stress intensity factor was $\sim$85–89% of the critical stress intensity factor under static (Fig. 11a) or dynamic (Fig. 11b) situation. Therefore, it emerges that the simplistic first-order understanding developed in the present work was in conformity with the more accurate predictions from earlier and recent rigorous micromechanical models and numerical simulations [60, 61]. Further, the picture proposed in the present work also

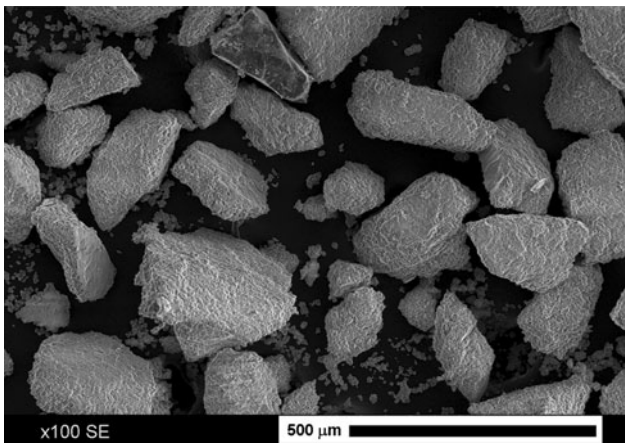

Fig. 12 Typical distribution of fragments obtained after the shock recovery experiments conducted at 6.5 GPa on the present alumina ceramics

matches with that of a very recent review work [62] on shock properties of ceramics.

Figure 12 shows a typical SEM photomicrograph of an assembly of fragments (size range 98 μm to about 275 μm, average ~163 μm) obtained after the shock recovery experiments. On the basis of the balance between the locally available kinetic energy during the impact event and the energy required to generate the new fragment surfaces, Grady [63] has very recently predicted the average macroscopic fragment size by the following equation:

$$\lambda = \left[\frac{\gamma}{\rho\left(\frac{\mathrm{d}\varepsilon}{\mathrm{d}t}\right)^2}\right]^{\frac{1}{3}} \tag{17}$$

where γ is fracture energy, ρ is density and $\left(\frac{\mathrm{d}\varepsilon}{\mathrm{d}t}\right)$ is the strain rate. Calculating γ as $\frac{K_{\mathrm{Ic}}^2}{\left[\frac{2E}{1-\nu^2}\right]}$, with $K_{\mathrm{Ic}} = 3.19$ MPa $\mathrm{m}^{0.5}$, $E =$ 400 GPa, $\nu = 0.27$ and putting $\rho = 3.978$ g cc^{-1}, $\left(\frac{\mathrm{d}\varepsilon}{\mathrm{d}t}\right) = 4 \times 10^4\ \mathrm{s}^{-1}$, an average fragment size $\lambda \sim 123$ μm is predicted. Thus, the predicted average macroscopic fragment size matched reasonably well with the experimental data.

Summary and conclusion

The Hugoniot elastic limit (HEL) of ~10 μm grain size coarse alumina ceramic was measured as ~2 GPa from symmetric shock experiments with a gas gun at 9.3 GPa shock pressure with 0.41 km s^{-1} impact velocity at a strain rate of $4 \times 10^4\ \mathrm{s}^{-1}$. The peak free surface velocity was 0.39 km s^{-1} while the dynamic yield strength was 1.2 GPa. An empirical linear dependence of HEL on grain size was found. Based on this HEL data, additional shock recovery experiments were conducted at 6.5 GPa (i.e. at a pressure of about 3.2 times the HEL) and the alumina fragments collected through a dedicated catcher system with a view to understand the deformation and fracture mechanisms. XRD studies with Rietveld analysis showed 57% decrease in crystallite size with a concomitant increase in average microstrain to 0.168 in the alumina fragments from 0.0843 in the control sample, confirming thereby the presence of a strained lattice. Nanoindentation experiments conducted for the first time on shock recovered alumina fragments confirmed that the average values of nanohardness and Young's modulus were reduced by about 15 and 27%, respectively, as compared to those of the control; presumably due to the presence of microcracks. SEM, FE-SEM and TEM characterization gave evidence for profuse presence of grain localized nano-scale deformations leading to formation of micro-cleavages, grain-boundary microcracks, stacking faults, dislocations, intra-granular shear deformation bands, localized agglomeration of 5–50 nm size debris smeared on fractured grain etc.; suggesting an important contribution from them to the overall damage initiation, incubation, sub-critical growth and later rapid failure propagation. Based on these evidences and existing literature a qualitative model was developed. The model suggests that apart from conventional large-scale macroscopic tensile and compressive fracture events, a major role is played by shear dominated failure. On impact of the shock wave, an increase of defect density takes place. As the shock wave propagation continues inside alumina, there may be shear as well as twist-induced micro-fracture initiation at a single plane or at multiple planes in a favourably oriented grain. These two processes can occur either independent to or concurrent with each other depending on which one is energetically more favourable. During the passage of the shock wave through the ceramic microstructure such unit events can many times repeat itself through a large multitude of individual grains and/or assembly of grains. As a result of these processes, multiple cracks grow, coalesce and propagate very fast to cause fragmentation and comminution of the microstructure. Finally it is shown that the experimentally measured fragment size matches with a theoretical estimate.

Acknowledgements The authors are grateful to Director, Central Glass and Ceramic Research Institute (CGCRI), Kolkata for his kind permission to publish this paper. In addition, the authors appreciate the infrastructural support received from Dr. J. Ghosh, Dr. S. Bysakh and all other colleagues and particularly those received from the colleagues of the Mechanical Property Evaluation Section at CGCRI. Finally, the authors gratefully acknowledge financial support received from the Board of Research in Nuclear Sciences, Department of Atomic Energy, Government of India and CSIR (Network Project Nos.: NWP 0027 and NWP 0029). One of the authors (A.D) also earnestly acknowledges the Grant of a Senior Research Fellowship from CSIR, India (ACK No.: 141011/2K8/2).

References

1. Bourne NK (2006) Proc R Soc A 462:3213
2. Chen MW, McCauley JW, Dandekar DP, Bourne NK (2006) Nat Mater 5:614
3. Murray NH, Bourne NK, Rosenberg Z (1998) J Appl Phys 84:4866
4. Ahrens TJ, Gust WH, Royce EB (1968) J Appl Phys 39:4610
5. Gust WH, Royce EB (1971) J Appl Phys 42:276
6. Longy F, Cagnoux J (1989) J Am Ceram Soc 72:971
7. Rosenberg Z, Brar NS, Bless SJ (1988) J Phys Colloques 49:707
8. Bourne NK, Rosenberg Z, Field JE, Crouch IG (1994) J Phys France IV 04:269
9. Staehler JM, Predebon WW, Pletka BJ (1994) AlP Conf Proc 309:745
10. O'Donnell RG (1991) J Mater Sci Lett 10:685
11. Wang Y, Mikkola DE (1992) J Am Ceram Soc 75:3252
12. Lankford J (1981) J Am Ceram Soc 64: C-33
13. Grady DE (1998) Mech Mater 29:181
14. Staehler JM, Predebon WW, Pletka BJ, Subhash G (2000) Mater Sci Eng A 291:37
15. Zaretsky EB, Kanel GI (2002) Appl Phy Lett 81:1192
16. Luo H, Chen W (2004) Int J Appl Ceram Technol 1:254
17. Bourne NK (2006) Proc R Soc A 462:3061
18. Zhang C, Kalia RK, Nakano A, Vashishta P (2007) Appl Phys Lett 91:071906
19. Zhang C, Kalia RK, Nakano A, Vashishta P (2007) Appl Phys Lett 91:121911
20. Dandekar DP, McCauley JW, Green WH, Bourne NK, Chen MW (2008) Report No A410974, Army Research Laboratory, Aberdeen Proving Ground MD, USA
21. Kanel GI, Zaretsky EB, Rajendran AM, Razorenov SV, Savinykh AS, Paris V (2009) Int J Plasticity 25:649
22. Gupta SC (1996) Indian J Pure Appl Phys 34:651
23. Gupta SC, Agarwal RG, Gyanchandani JS, Roy S, Suresh N, Sikka SK, Kakodkar A, Chidambaram R (1992) In: Schmidt SC, Dick RD, Forbes JW, Tasker DG (eds) Shock compression of condensed matter-1991. Elsevier, Amsterdam, pp 839–842
24. Zaretsky EB, Kanel GI, Razorenov SV, Baumung K (2005) Int J Impact Eng 31:41
25. Joshi KD, Rav A, Gupta SC (2008) Proceedings of Interquadrennial Conference of International Congress on Fracture. pp 164–166
26. Oliver WC, Pharr GM (1992) J Mater Res 7:1564
27. Bourne NK, Rosenberg Z, Crouch IG, Field JE (1994) Proc Royal Soc London A 446:309
28. Rice RW (2000) Mechanical properties of ceramics and composites: grain and particle effects. CRC Press, New York
29. Knudsen FP (1959) J Am Ceram Soc 42:376
30. Griffith AA (1920) Phil Trans R Soc London A221:163
31. Petch NJ (1953) J Iron Steel Inst 174:25
32. Mukhopadhyay AK, Joshi KD, Biswas S, Bhattacharya S, Ghosh J, Bysakh S, Rav A, Gupta SC (2009) Proceeding of MRSI-AGM symposium, Kolkata, 10–12 February, p 57
33. Mukhopadhyay AK, Joshi KD, Biswas S, Bhattacharyya S, Rav A, Gupta SC (2008) Proceeding of DAE solid state physics symposium, Mumbai, 16–20 December, pp 745–746
34. Chen M, McCauley JW, Hemker KJ (2003) Science 299:1563
35. Shih CJ, Meyers A, Nesterenko VF (1998) Acta Mater 46:4037
36. Lankford J, Predebon WW, Staehler JM, Subhash G, Pletka BJ, Andersona CE (1998) Mech Mater 29:205
37. Kaplan WD, Kenway PR, Brandon DG (1995) Acta Metall Mater 43:835
38. Shih CJ, Meyers MA, Nesterenko VF, Chen SJ (2000) Acta Mater 48:2399
39. Johnson GR, Holmquist TJ (1994) High-pressure science and technology. American Institute of Physics, New York
40. Partom Y (1993) Technical report IAT.TN.006. Inst. for Advanced Technology
41. Fahrenthold EP (1991) J Appl Mech 58:904
42. Rajendran AM, Grove DJ (1992) Proceedings of the 24th international SAMPE technical conference allied signals, Oct. 1992
43. Curran DR, Seaman L, Cooper T, Schockey DA (1993) Int J Impact Eng 13:53
44. Espinosa HD (1992) PhD Thesis, Brown University, USA
45. Camacho GT, Ortiz M (1996) Int J Solids Struct 33:2899
46. Ortiz M (1996) Comput Mech 18:321
47. Espinosa HD, Zavattieri PD, Dwivedi SK (1998) J Mech Phys Solids 46:1909
48. Espinosa HD (1995) Int J Solids Struct 32:3105
49. Bourne NK (2002) Proc R Soc Lond A 458:1999
50. Simhaa CHM, Blessa SJ, Bedford A (2002) Int J Impact Eng 27:65
51. Horii M, Nemat-Nasser S (1986) Phil Trans R Soc Lond A 319:337
52. Warner DH, Molinari JF (2006) Acta Mater 54:5135
53. Lu Z, Nomura KI, Sharma A, Wang W, Zhang C, Nakano A, Kalia R, Vashishta P (2005) Phy Rev Lett 95:135501
54. Leme-Louro LH, Meyers MA (1989) In: Proc Am Phys Soc Topic Conf shock compression of condensed matter, pp 464–468
55. Li X, Xu ZH, Wang R (2006) Nano Lett 6:2301
56. Strassburger E, Senf H, Rothenhaeuler H (1994) J De Physique IV 4:653
57. Fukuhara M, Yamauchi I (1993) J Mater Sci 29:4681. doi: 10.1007/BF00414258
58. Suresh S, Nakamura T, Yeshurun Y, Yang KH, Duffy J (1990) J Am Ceram Soc 73:2457
59. LaSalvia JC (2002) Ceram Eng Sci Proc 23:213
60. Ravichandran G, Subhash G (1995) lnt J Solids Struct 32:2627
61. Huang C, Subhash G (2003) J Mech Phys Solids 51:1089
62. Walley SM (2009) Adv Appl Ceram (in press). doi:10.1179/174367609X422180)
63. Grady DE (2008) Int J Impact Eng 35:1557